International Journal of Mechanical Sciences 134 (2017) 85–97

Contents lists available at ScienceDirect

International Journal of Mechanical Sciences

journal homepage: www.elsevier.com/locate/ijmecsci

Melting of nanoparticles-enhanced phase-change materials in an enclosure: Effect of hybrid nanoparticles

Mohammad Ghalambaz[a,*], Ali Doostani[a], Ali J. Chamkha[b,c], Muneer A. Ismael[d]

[a] Department of Mechanical Engineering, Dezful Branch, Islamic Azad University, Dezful, Iran
[b] Mechanical Engineering Department, Prince Mohammad Bin Fahd University, Al-Khobar 31952, Saudi Arabia
[c] Prince Sultan Endowment for Energy and Environment, Prince Mohammad Bin Fahd University, Al-Khobar 31952, Saudi Arabia
[d] Mechanical Engineering Department, Engineering College, University of Basrah, Basrah, Iraq

ARTICLE INFO

Keywords:
Phase-change material
Hybrid nanofluid
Cavity
Melting
Enthalpy-porosity model

ABSTRACT

The present paper studies the melting of nanoparticles-enhanced phase-change materials (NEPCM) in a square cavity using the finite element method. The enhancement is based on the hybrid nanofluid strategy. A linearized correlations procedure has been followed to determine the properties of the hybrid nanofluid. The Rayleigh, Prandtl, and Stefan numbers have been fixed at 10^8, 50, and 0.1, respectively. The left wall is kept at a higher temperature $T_h = 40\,^{\circ}C$, the right wall is kept at a lower temperature $T_c = 30\,^{\circ}C$, while the horizontal walls are kept adiabatic. The enthalpy-porosity model is used to simulate the melting of the phase-change materials (PCM). The study is governed by tracing the liquid–solid interface by varying the total nanoparticles volume fraction $\phi = 0$–5%, and four different sets of models parameters combinations (Nc, Nv) = (0,0), (5,18), (18,18), (18,5). The results have shown the consistency of the liquid–solid phase progress with the available experimental results, i.e. the melting process expedites when the enhancement in the thermal conductivity, which is characterized by Nc, is much greater than the enhancement of the dynamic viscosity. Compared with the available experimental data, hybrid nanoparticles composed of Mg–MgO demonstrate the best fusion performance.

1. Introduction

Our life testifies rapid development in the electronics and engineering industries which is accompanied with high cooling and conditioning requirements. These requirements may need a larger attention to be satisfied. On the other hand, there are transcendent voices of preserving the environment. Alternative techniques which compromise between all of these requirements are, therefore, necessary. Phase-change materials (PCM) are one of the efficient topics for these demands. They are classified as substances of high latent heat because heat is absorbed or released when they melt and solidify at a certain temperature. In other words, they have the capability of storing or releasing large amounts of energy, and thus, they are termed as thermal energy storage material. Within a small temperature difference, they can be rapidly and repeatedly switched between the liquid–solid phases. They are widely used in many industrial applications such as heat exchangers, solar energy, cooling of electric and combustion engines, refrigeration and air conditioning, and many other applications [1].

Phase-change materials were addressed in the early works of Telkes and Raymond [2] in 1949. However, they did not find real interest at that time. Due to the continuously increasing demands for energy, Telkes [3–5] had developed this field of investigation to the issue we know today. As such, this topic has attracted many review attention regarding the general applications, types, and preparation of PCMs [6–9]. Other reviews have focused on the techniques of improving the relatively low thermal conductivity of PCMs [10,11]. Early reviews regarding the mathematical and numerical treatments of the problem can be found in [12,13].

The thermal energy storage in PCMs contained in different flow geometries and enclosures has attracted the attention of many researchers. Ebrahimnia-Bajestan et al. [14] concluded that increasing the Rayleigh number could reduce the freezing time while the water content in the food can extend the freezing time. The experiments of Allen et al. [15] have concluded that an enhanced system combined of a heat pipe with foils or foam may achieve much higher melting and solidification rates with respect to a non-enhanced system. Mirzaei et al. [16] concluded that using proper arrangement of discrete heat sources had a great potential for improving the energy storage system of a melting process of a PCM in a 2-D horizontal cylindrical annulus. Kousksou et al. [17] studied numerically the melting process along a vertical wavy

* Corresponding author.
E-mail addresses: m.ghalambaz@iaud.ac.ir, m.ghalambaz@gmail.com (M. Ghalambaz), adoostani@mpc.ir, doostaniali@gmail.com (A. Doostani), achamkha@pmu.edu.sa (A.J. Chamkha), muneer.ismael.ecb@uobasrah.edu.iq (M.A. Ismael).

https://doi.org/10.1016/j.ijmecsci.2017.09.045
Received 21 September 2016; Received in revised form 10 September 2017; Accepted 25 September 2017
Available online 3 October 2017
0020-7403/

Nomenclature

A_{mush}	mushy-zone constant (Carman–Koseny equation constant)
C	specific heat (J/kg K)
C_p	specific heat in constant pressure (J/kg K)
g	gravity (m/s^2)
H	length and Height (m)
k	thermal conductivity (W/m K)
L	latent heat of fusion (J/kg)
Nc	conductivity parameter
$N\upsilon$	viscosity parameter
P	pressure (Pa)
Pr	Prandtl number
Ra	Rayleigh number
$S(T)$	Carman–Kozeny equation (source term)
Ste	Stefan number
T	temperature (K)
T_f	melting temperature (K)
t	time
u	velocity in the x-direction (m/s)
v	velocity in the y-direction (m/s)
x, y	Cartesian coordinates

Greek symbols

α	thermal diffusivity (m^2/s)
β	thermal expansion coefficient (1/K)
γ	the ratio of thermal diffusivity
ΔT	mushy-zone temperature range (K)
ε	Carman–Kozeny equation constant
θ	non-dimensional temperature
μ	dynamic viscosity (kg/m s)
ξ	basis functions
ρ	density (kg/m^3)
ν	kinematic viscosity (m^2/s)
$\varphi(T)$	liquid fraction
ϕ	volume fraction of nanoparticles

subscripts

hnf	hybrid nanofluid
l	liquid phase
nf	nanofluid
F	fusion
s	solid

surface with uniform surface temperature. They found that the rate of the melting increased with the increase of the amplitude of the wavy surface. Bondareva and Sheremet studied the effect of the presence of a local heat source on the melting behavior of a phase-change material in a square cavity [18]. Following [18], Bondareva and Sheremet [19,20] addressed the effects of the presence of a uniform inclined magnetic field on the natural convection heat transfer combined with the melting process in a square cavity [19] and cubical cavity [20].

Generally, the thermal conductivity can be increased either by redesigning the geometry of PCM containers, or by an additive of nanoparticles or nanotubes. Tiari et al. [21–23] investigated numerically the thermal characteristics of a finned heat pipe-assisted latent heat thermal energy storage system. The increase of the fin length resulted in providing more uniform temperature distribution. Sari and Karaipekli [24] prepared a phase-change material composite of paraffin absorbed into expanded graphite that enhanced the thermal conductivity which in turn, reduced the melting time. Motahar et al. [25] have addressed the solidification process of a phase-change material containing TiO_2 nanoparticles for thermal energy storage. Dhaidan [26] have reviewed the analytical, numerical and experimental investigations of NePCM and addressed the effect of the cavity geometry on the melting behavior of the nanostructures-assisted phase-change materials. Dhaidan [26] concluded that the measured actual thermophysical properties of NePCM should be utilized in numerical investigations instead of depending on simple mixture models. Şahan et al. [27] prepared paraffin–non magnetite (Fe_3O_4) composites (PNMC) by a dispersion technique to enhance their thermal properties. Their results demonstrated that the addition of Fe_3O_4 nanoparticles is an efficient and cost effective method to enhance the heat transfer properties of paraffin, when they are incorporated into latent heat storage systems. Kashani et al. [28] and Abdollahzadeh and Esmaeilpour [29] made two separate studies on solidification of Cu-water nanofluid in wavy cavities. They reported that the nanoparticles additions could decrease the solidification times. However, the wall waviness can control the solidification process. Jorabian and Farhadi [30] examined numerically the melting process of Cu-water nanofluids in PCMs in a semi-circle enclosure using the enthalpy-based Lattice Boltzman method. They showed that the increase in the volume fraction of nanoparticles resulted in the enhancement of the thermal conductivity of PCM and the decrease in the latent heat of fusion. The numerical study of Sharma et al. [31] on the solidification of the Cu-water showed that the heat transfer performance of NEPCM was significantly enhanced with the use of a trapezoidal cavity when compared to a square cavity having the same internal area. However, abundant papers have been published and continue to be published on dispersing of nanoparticles in order to improve the thermal performance of PCMs, see for examples the experimental works [32–37], and the analytical works [38–40].

However, most of the numerical studies regarding nanoparticles-enhanced PCM indicate decreases in the solidification times and increases in the melting times as a result of increasing the nanoparticles volume fraction [29]. Nevertheless, the experimental results demonstrate a contrast behavior of the NEPCM, where Zeng et al. [34] have demonstrated an acceleration in the melting times when multi-walled carbon nanotubes is dispersed in 1-dodeconal. They attributed this discrepancy to uncertainties of the models of the thermo-physical properties of NEPCMs that had been used in the numerical studies. As such, they suggested the use of the measured thermo-physical properties instead of those predicted using simple mixture models or correlations.

Recently, a very new class of nanofluids obtained by suspending different nanoparticles called “hybrid” nanofluids is slowly growing as an investigation field. Compromised properties between the advantages and disadvantages properties of individual nanoparticles are a declared task of hybridization. Moreover, we found that the nanoparticles suppliers exhibit noticeable differences in prices of different nanoparticles types. For example, the price of copper nanoparticles is about 10 times greater than that of alumina nanoparticles. Hence, it is appropriate if one achieves the benefits of the expensive nanoparticles properties with minimum quantity.

Indeed, the “hybrid” nanoparticles should be limited to those prepared as a single composite substance in the base fluid for which their synthetization requires extra attention [41–43]. However, the “hybrid” topic is also used to those prepared by suspending dissimilar nanoparticles types in a base fluid. Comprehensive details of hybrid nanoparticles synthesis are reviewed in Sarkar et al. [44]. This review shows very limited studies concerning the mathematical models of the hybrid nanofluids properties. For example, the experiments of Ho et al. [45] showed very good agreements between the measured data of the density and mass fraction (ρ, Cp) and those predicted using the mixture theory. Their experiments were based on suspensions of Al_2O_3 nanoparticles and particles of micro-encapsulated phase-change material in water as a base fluid. Nevertheless, the experiments of Botha et al. [46], which were conducted on silver–silica-oil-based hybrid nanofluid showed that the Maxwell relation [47] underestimates the thermal conductivity with more deviation at higher solid volume fractions. Sebti et al. [48] have studied the melting of Cu-paraffin phase-change material in a square cavity for various volume fractions of copper nanoparticles.

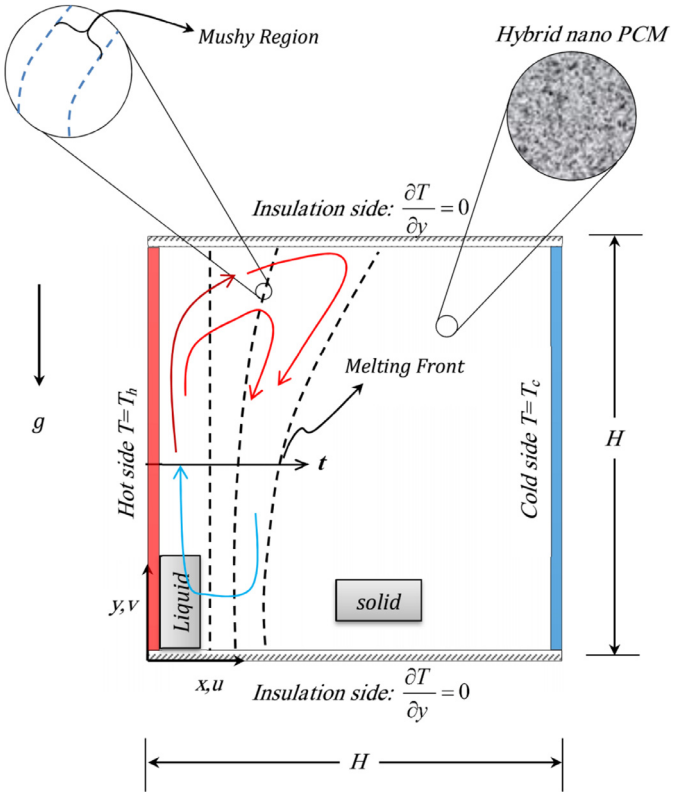

Fig. 1. A schematic diagram of the physical model and geometry details.

According to the above literature survey, we ascertain that the hybrid nanofluid in phase-change materials has not been investigated yet. Thus, the present paper aims to address the effect of dispersing hybrid nanoparticles in PCMs contained in a square cavity. The melting behavior together with the thermal and flow fields will be traced for this purpose.

2. Physical and mathematical modeling

Consider a square enclosure of side H filled by a phase-change material (PCM). Initially, the PCM is considered a frozen substance (solid). The left side wall of the enclosure is kept isothermal at a hot temperature T_h and the right wall is kept isothermal at a cold temperature T_c while the top and bottom walls are thermally insulated. A schematic representation of the cavity, coordinate system and the physical model are depicted in Fig. 1. Hybrid nanoparticles are dispersed in the PCM. After melting, the thermo-physical properties in each phase are assumed to be constant. The thermo-physical properties of the hybrid nanofluid (liquid phase) are assumed to be constant except for the density where the Boussinesq approximation is applicable. No-slip between the hybrid nanoparticles and the liquid is considered. The flow in the liquid phase is assumed laminar, incompressible and Newtonian. It is also assumed that Joule heating effects as well as the viscous dissipation effects and radiation effects are negligible. According to the above assumptions, the conservation equations for mass, momentum and energy are written as:

Continuity

$$\frac{\partial u}{\partial x}+\frac{\partial v}{\partial y}=0 \tag{1}$$

Momentum in x-direction

$$\rho_{hnf}\left(\frac{\partial u}{\partial t}+u\frac{\partial u}{\partial x}+v\frac{\partial u}{\partial y}\right)=-\frac{\partial p}{\partial x}+\left(\frac{\partial}{\partial x}\left(\mu_{hnf}(\varphi)\frac{\partial u}{\partial x}\right)+\frac{\partial}{\partial y}\left(\mu_{hnf}(\varphi)\frac{\partial u}{\partial y}\right)\right)+S(T).u \tag{2}$$

Momentum in y-direction

$$\rho_{hnf}\left(\frac{\partial u}{\partial t}+u\frac{\partial v}{\partial x}+v\frac{\partial v}{\partial y}\right)=-\frac{\partial p}{\partial y}+\left(\frac{\partial}{\partial x}\left(\mu_{hnf}(\varphi)\frac{\partial v}{\partial x}\right)+\frac{\partial}{\partial y}\left(\mu_{hnf}(\varphi)\frac{\partial v}{\partial y}\right)\right)+g(\rho\beta)_{hnf}\left(T-T_f\right)+S(T).v \tag{3}$$

Energy

$$\left(\frac{\partial T}{\partial t}+u\frac{\partial T}{\partial x}+v\frac{\partial T}{\partial y}\right)=-\frac{1}{(\rho C_P)_{hnf}}\left(\frac{\partial}{\partial x}\left(k_{hnf}\alpha(\varphi)\frac{\partial T}{\partial x}\right)+\frac{\partial}{\partial y}\left(k_{hnf}\alpha(\varphi)\frac{\partial T}{\partial y}\right)\right)+\frac{L}{(C_P)_{hnf}}\frac{\partial\varphi(T)}{\partial t} \tag{4}$$

The thermal diffusivity is defined as:

$$\alpha(\varphi)=\alpha_{l,hnf}\varphi+\alpha_{s,hnf}(1-\varphi) \tag{5}$$

where φ is the melt fraction which is evaluated using the temperature as:

$$\varphi(T)=\begin{cases}0 & T<T_f\\ \frac{T-T_f}{\Delta T} & T_f<T<T_f+\frac{\Delta T}{2}\\ 1 & T>T_f+\Delta T\end{cases} \tag{6}$$

ΔT is the mushy-zone temperature range.

The dynamic viscosity is also controlled in the mushy region using the following relation:

$$\mu(\varphi)=\mu_l\left(1+A_{mush}(1-\varphi)\right) \tag{7}$$

It should be noted that as a consequence of using Eq. (7) for the viscosity in the mushy region, the pressure and the velocity fields in the domain of the solution become uniform and the velocity field takes on the value zero close to the solid parts of the domain. As mentioned before, the thermal diffusivity in the liquid, mushy and solid regions is a linear function of the volume fraction of the liquid given by Eq. (5).

The source term $S(T)$ in the momentum equation is modeled as a continuous equation for phase transition using the Carman–Kozeny equation:

$$S(T)=-A_{mush}\frac{(1-\varphi(T))^2}{\varphi(T)^3+\varepsilon} \tag{8}$$

The Physical boundary conditions for the problem under consideration are given by:

$$\text{Heated wall}\quad x=0,\quad y=y:\quad u=0,\quad v=0,\quad T_s=T_h \tag{9a}$$

$$\text{Cooled wall}\quad x=H,\quad y=y:\quad u=0,\quad v=0,\quad T=T_c \tag{9b}$$

$$\text{Top wall}\quad x=x,\quad y=H:\quad u=0,\quad v=0,\quad \frac{\partial T}{\partial y}=0 \tag{9c}$$

$$\text{Bottom wall}\quad x=x,\quad y=0\quad u=0,\quad v=0,\quad \frac{\partial T}{\partial y}=0 \tag{9d}$$

where H is the width and height of the square enclosure.

It is convenient to non-dimensionalize Eqs. (1)–(4) using the following dimensionless variables:

$$X=\frac{x}{H},\quad Y=\frac{y}{H},\quad U=\frac{uH}{\alpha_{l,bf}},\quad V=\frac{vH}{\alpha_{l,bf}},\quad \theta=\frac{T-T_f}{T_h-T_f},\quad AR=\frac{R}{L} \tag{10}$$

$$Fo=\frac{t\alpha_{bf}}{H^2},\quad S(\theta)=\frac{s(T)H^2}{\rho_{l,hnf}\alpha_{l,bf}},\quad \mu_r=\frac{\mu_{hnf}(\varphi)}{\mu_{bf}}\alpha_r=\frac{\alpha_{hnf}(\varphi)}{\alpha_{bf}},\quad P=\frac{PH^2}{\rho_{l,bf}\alpha_{l,bf}^2} \tag{11}$$

Through the non-dimensionalization process, the following important dimensionless parameters are obtained:

$$Ra = \frac{g\beta_{bf}(T_h - T_f)L^3}{\alpha_{l,bf}\upsilon_{bf}}, \quad \text{Ste} = \frac{C_{l,bf}(T_h - T_f)}{L_{bf}}, \quad Pr = \frac{\upsilon_{bf}}{\alpha_{l,bf}} \tag{12}$$

where Ra is the Rayleigh number, Ste is the Stefan number, and Pr is the Prandtl number

By substituting Eqs. (10) and (11) into Eqs. (1)–(4), one obtains the following non-dimensional governing equations:

Continuity:

$$\frac{\partial U}{\partial X} + \frac{\partial V}{\partial Y} = 0 \tag{13}$$

Momentum in X-direction:

$$\frac{\partial U}{\partial Fo} + U\frac{\partial U}{\partial X} + V\frac{\partial U}{\partial Y} = -\frac{\rho_{bf}}{\rho_{hnf}}\frac{\partial P}{\partial X} + \frac{\rho_{bf}}{\rho_{hnf}}\frac{\mu_{hnf}}{\mu_{bf}}Pr\left(\frac{\partial}{\partial X}\left(\mu_r\frac{\partial U}{\partial X}\right) + \frac{\partial}{\partial Y}\left(\mu_r\frac{\partial U}{\partial Y}\right)\right) + \frac{\rho_{bf}}{\rho_{hnf}}S(\theta)U \tag{14}$$

Momentum in Y-direction:

$$\frac{\partial V}{\partial Fo} + U\frac{\partial V}{\partial X} + V\frac{\partial V}{\partial Y} = -\frac{\rho_{bf}}{\rho_{hnf}}\frac{\partial P}{\partial Y} + \frac{\rho_{bf}}{\rho_{hnf}}\frac{\mu_{hnf}}{\mu_{bf}}Pr\left(\frac{\partial}{\partial X}\left(\mu_r\frac{\partial V}{\partial X}\right) + \frac{\partial}{\partial Y}\left(\mu_r\frac{\partial V}{\partial Y}\right)\right) + \frac{\rho_{bf}}{\rho_{hnf}}S(\theta)V + PrRa\theta\frac{(\rho\beta)_{hnf}}{\rho_{hnf}\beta_{bf}} \tag{15}$$

Energy:

$$\frac{\partial \theta}{\partial Fo} + U\frac{\partial \theta}{\partial X} + V\frac{\partial \theta}{\partial Y} = \left(\frac{\partial}{\partial X}\left(\frac{\alpha_{hnf}(\varphi)}{\alpha_{l,bf}}\frac{\partial \theta}{\partial X}\right) + \frac{\partial}{\partial Y}\left(\frac{\alpha_{hnf}(\varphi)}{\alpha_{l,bf}}\frac{\partial \theta}{\partial Y}\right)\right) - \frac{(C_p)_{bf}}{(C_p)_{hnf}}(1-\varphi)\frac{1}{Ste}\frac{\partial \varphi(\theta)}{\partial Fo} \tag{16}$$

where U, V, C, P and T are the x-velocity, y-velocity, volume fraction of nanoparticles, pressure and the temperature of the nanofluid, respectively. The subscripts *hnf*, *bf* and *p* denote the hybrid nanofluid, the base fluid and the nanoparticles, respectively.

It should be noted that in Eq. (16), the thermal diffusivity ratio can be evaluated as

$$\frac{\alpha_{hnf}(\varphi)}{\alpha_{l,bf}} = \left(\frac{\varphi k_{l,hnf} + (1-\varphi)k_{s,hnf}}{k_{l,bf}}\right)\frac{\varphi C_{p_{l,hnf}} + (1-\varphi)C_{p_{s,hnf}}}{C_{p_{l,bf}}} \tag{17}$$

Following Eq. (17), the non-dimensional form of the viscosity equation, Eq. (7) can be evaluated as follows:

$$\mu_r = \left(1 + A_{mush}(1-\varphi)\right) \tag{18}$$

Eqs. (13)–(16) are subjected to the following boundary conditions and by using the variables in Eq. (10), the non-dimensional boundary conditions are:

$$\text{Heated wall} \quad X = 0: \quad U = 0, \quad V = 0, \quad \theta_s = 1 \tag{19a}$$

$$\text{Cooled wall} \quad X = 1: \quad U = 0, \quad V = 0, \quad \theta_s = 0 \tag{19b}$$

$$\text{Top wall} \quad Y = AR: \quad U = 0, \quad V = 0, \quad \frac{\partial \theta}{\partial Y} = 0 \tag{19c}$$

$$\text{Bottom wall} \quad Y = 0: \quad U = 0, \quad V = 0, \quad \frac{\partial \theta}{\partial Y} = 0 \tag{19d}$$

The melt volume fraction as a function of θ is written as:

$$\varphi(\theta) = \begin{cases} 0 & \theta < 0 \\ \frac{\theta}{\Delta\theta} & 0 < \theta < \Delta\theta \\ 1 & \theta > \Delta\theta \end{cases} \tag{20}$$

where $\Delta\theta = \frac{\Delta T}{T_h - T_f}$. The initial temperature in the non-dimensional form is evaluated as $\theta = 0$ in the cavity.

Because there is no published sophisticated numerical models for hybrid nanofluid properties, we followed the procedure proposed by Zarki et al. [49]. This procedure linearizes the properties based on experimental data documented by other experimental studies, and as follows:

$$\frac{\mu_{hnf}}{\mu_{bf}} = (1 + Nv \times \phi) \tag{21}$$

$$\frac{k_{hnf}}{k_{bf}} = (1 + Nc \times \phi) \tag{22}$$

$$\frac{\alpha_{hnf}}{\alpha_{bf}} = \frac{k_{hnf}}{k_{bf}}\frac{(\rho c_p)_{bf}}{(\rho c_p)_{hnf}} \tag{23}$$

Following the experimental study of Esfe et al. [50] and the theoretical study of Zarki et al. [49], the magnitudes of ρ_{bf}/ρ_{hnf}, $(\rho C_p)_{bf}/(\rho C_p)_{hnf}$, C_{bf}/C_{hnf} and $\rho_{bf}\beta_{bf}/(\rho\beta)_{hnf}$ for most of nanofluids are about unity. Indeed, by using nanoparticles in the base fluid, only the thermal conductivity and the dynamic viscosity of the resulting nanofluid would change dramatically. Therefore, by considering $(\rho C_p)_{bf}/(\rho C_p)_{hnf} \approx 1$ and using Eq. (23), the thermal diffusivity ratio α_{hnf}/α_{bf} can be simplified as

$$\frac{\alpha_{hnf}}{\alpha_{bf}} = \frac{k_{hnf}}{k_{bf}}\frac{(\rho C_P)_{bf}}{(\rho C_P)_{hnf}} = (1 + Nc \times \phi) \times (\approx 1) = 1 + Nc \times \phi \tag{24}$$

Thus, in the present study, ρ_{bf}/ρ_{hnf}, $(\rho C_p)_{bf}/(\rho C_p)_{hnf}$, C_{bf}/C_{hnf} and $\rho_{hnf}\beta_{bf}/(\rho\beta)_{hnf}$ are considered as equal to unity. The reason that the thermo-physical properties have been assumed to be constant is to simplify the problem with eliminating the variables that have less effect on the overall solution. In the work of Zaraki et al. [49], it was discussed that the effect of the presence of a very low volume fraction of nanoparticles on the dynamic viscosity and thermal conductivity is significant and the change in the other thermo-physical properties would be very smooth. Hence, in the present study, we assumed that the dominant variation of the thermo-physical properties is due to the thermal conductivity and the dynamic viscosity of nanofluids and that the other thermophysical properties have minor roles.

The stored or released latent heat is a direct function of the melting volume fraction of the PCM. As mentioned, use of nanoparticles can reduce the latent heat of the phase-change material. Thus, using the following relation, the stored latent heat of NEPCM can be evaluated using the volume fraction curves of NEPCMs:

$$\frac{Q}{L} = (1 - \phi) \times Liquid\ fraction \tag{25}$$

As mentioned, the presence of nanoparticles does not show a significant effect on the heat capacity of NEPCMs. Moreover, it is found that the presence of nanoparticles would smoothly change the temperature gradient in the molten region. Thus, a little change in the sensible heat of NEPCM due to the presence of nanoparticles can be expected.

3. Numerical solution

The system of partial differential Eqs. (13)–(16) along with the boundary conditions, Eq. (19), are transformed into the weak form and are solved numerically using the Galerkin finite element method [51]. The computer solution codes associated with user-defined MATLAB subroutines were adopted to solve the system of the governing equations. The continuity equation (Eq. (13)) is employed as a constraint to satisfy the mass conservation by controlling the pressure distribution. Thus, the following constraint equation is utilized as a penalty parameter (χ) in the momentum equations as described by Reddy [51]. Therefore, the pressure is written as

$$P = \chi\left(\frac{\partial U}{\partial X} + \frac{\partial V}{\partial Y}\right) \tag{26}$$

where χ is the penalty number, which is a large value. Using Eq. (26), the momentum Eqs. (14) and (15) are written as:

$$\frac{\partial U}{\partial Fo}+U\frac{\partial U}{\partial X}+V\frac{\partial U}{\partial Y}=-\frac{\rho_{bf}}{\rho_{hnf}}\frac{\partial}{\partial X}\left(\chi\left(\frac{\partial U}{\partial X}+\frac{\partial V}{\partial Y}\right)\right)+\frac{\rho_{bf}}{\rho_{hnf}}\frac{\mu_{hnf}}{\mu_{bf}}Pr\left(\frac{\partial}{\partial X}\left(\mu_r\frac{\partial U}{\partial X}\right)+\frac{\partial}{\partial Y}\left(\mu_r\frac{\partial V}{\partial Y}\right)\right)+\frac{\rho_{bf}}{\rho_{hnf}}S(\theta)U \tag{27}$$

$$\frac{\partial V}{\partial Fo}+U\frac{\partial V}{\partial X}+V\frac{\partial V}{\partial Y}=-\frac{\rho_{bf}}{\rho_{hnf}}\frac{\partial}{\partial Y}\left(\chi\left(\frac{\partial U}{\partial X}+\frac{\partial V}{\partial Y}\right)\right)+\frac{\rho_{bf}}{\rho_{hnf}}\frac{\mu_{hnf}}{\mu_{bf}}Pr\left(\frac{\partial}{\partial X}\left(\mu_r\frac{\partial U}{\partial X}\right)+\frac{\partial}{\partial Y}\left(\mu_r\frac{\partial V}{\partial Y}\right)\right)+\frac{\rho_{bf}}{\rho_{hnf}}S(\theta)V+PrRa\theta\frac{(\rho\beta)_{hnf}}{\rho_{hnf}\beta_{bf}} \tag{28}$$

Thus, in the above equations, the continuity Eq. (13) is satisfied for very large values of the penalty parameter ($\chi = 10^7$) [51]. Now, the velocities (U and V) as well as the temperature, θ, are expanded by invoking a basis set $\{\xi_k\}_{k=1}^{N}$ in the domain interval of $-0.5 < X < 0.5$ and $0 < Y < 1$ as,

$$U\approx\sum_{k=1}^{N}U_k\xi(X,Y),\ V\approx\sum_{k=1}^{N}k_k\xi(X,Y),\ \theta\approx\sum_{k=1}^{N}\theta_k\xi(X,Y) \tag{29}$$

It is worth noting that the basis function ζ is the same for all of the three variables. Therefore, the total number of nodes is $N = 3$. Invoking the introduced basis functions Eq. (29)), the nonlinear residual equations ($R^N{}_i$) of the governing momentum Eqs. (27) and ((28) together with the energy Eq. (16) can be derived as follows:

$$R_i^1=\sum_{k=1}^{N}U_k\int_\Omega\frac{\partial\xi_k}{\partial Fo}\xi_i dXdY+\sum_{k=1}^{N}U_k\int_\Omega\left[\left(\sum_{k=1}^{N}U_k\xi_k\right)\frac{\partial\xi_k}{\partial X}+\left(\sum_{k=1}^{N}V_k\xi_k\right)\frac{\partial\xi_k}{\partial Y}\right]\xi_i dXdY+\frac{\rho_{bf}}{\rho_{hnf}}\left(\sum_{k=1}^{N}U_k\int_\Omega\frac{\partial\xi_i}{\partial X}\left[(\chi)\frac{\partial\xi_k}{\partial X}dXdY\right]+\sum_{k=1}^{N}V_k\int_\Omega\frac{\partial\xi_i}{\partial X}\left[(\chi)\frac{\partial\xi_k}{\partial Y}dXdY\right]\right)+\frac{\rho_{bf}}{\rho_{hnf}}\frac{\mu_{hnf}}{\rho_{bf}}Pr\left[\sum_{k=1}^{N}U_k\int_\Omega\frac{\partial\xi_i}{\partial X}\left(\mu_r\frac{\partial\xi_k}{\partial X}dXdY\right)+\sum_{k=1}^{N}U_k\int_\Omega\frac{\partial\xi_i}{\partial Y}\left(\mu_r\frac{\partial\xi_k}{\partial Y}dXdY\right)\right]+\frac{\rho_{bf}}{\rho_{hnf}}S(\theta)\sum_{k=1}^{N}\int_\Omega\left(\sum_{k=1}^{N}(U_k\xi_k)\xi_i\right)dXdY \tag{30}$$

$$R_i^2=\sum_{k=1}^{N}V_k\int_\Omega\frac{\partial\xi_k}{\partial Fo}\xi_i dXdY+\sum_{k=1}^{N}V_k\int_\Omega\left[\left(\sum_{k=1}^{N}U_k\xi_k\right)\frac{\partial\xi_k}{\partial X}+\left(\sum_{k=1}^{N}V_k\xi_k\right)\frac{\partial\xi_k}{\partial Y}\right]\xi_i dXdY+\frac{\rho_{bf}}{\rho_{hnf}}\left(\sum_{k=1}^{N}U_k\int_\Omega\frac{\partial\xi_i}{\partial Y}\left[(\chi)\frac{\partial\xi_k}{\partial X}dXdY\right]+\sum_{k=1}^{N}V_k\int_\Omega\frac{\partial\xi_i}{\partial Y}\left[(\chi)\frac{\partial\xi_k}{\partial Y}dXdY\right]\right)+\frac{\rho_{bf}}{\rho_{hnf}}\frac{\mu_{hnf}}{\rho_{bf}}Pr\left[\sum_{k=1}^{N}V_k\int_\Omega\frac{\partial\xi_i}{\partial X}\left(\mu_r\frac{\partial\xi_k}{\partial X}dXdY\right)+\sum_{k=1}^{N}V_k\int_\Omega\frac{\partial\xi_i}{\partial Y}\left(\mu_r\frac{\partial\xi_k}{\partial Y}dXdY\right)\right]+\frac{(\rho\beta)_{hnf}}{\rho_{hnf}\beta_{bf}}RaPr\left[\int_\Omega\left(\sum_{k=1}^{N}\theta_k\xi_k\right)\xi_i dXdY\right]+\frac{\rho_{bf}}{\rho_{hnf}}S(\theta)\sum_{k=1}^{N}\int_\Omega\left(\sum_{k=1}^{N}(V_k\xi_k)\xi_i\right)dXdY \tag{31}$$

$$R_i^3=\sum_{k=1}^{N}\theta_k\int_\Omega\frac{\partial\xi_k}{\partial Fo}\xi_i dXdY+\sum_{k=1}^{N}\theta_k\int_\Omega\left[\left(\sum_{k=1}^{N}U_k\xi_k\right)\frac{\partial\xi_k}{\partial X}+\left(\sum_{k=1}^{N}V_k\xi_k\right)\frac{\partial\xi_k}{\partial Y}\right]\xi_i dXdY+\frac{\alpha_{bf}}{\alpha_{hnf}}\left(\sum_{k=1}^{N}\theta_k\int_\Omega\frac{\partial\xi_i}{\partial X}\left[\alpha_r\frac{\partial\xi_k}{\partial X}dXdY\right]+\sum_{k=1}^{N}\theta_k\int_\Omega\frac{\partial\xi_i}{\partial Y}\left[\alpha_r\frac{\partial\xi_k}{\partial Y}dXdY\right]\right)+\frac{(C_p)_{bf}}{(C_p)_{hnf}}\frac{1}{Ste}\sum_{k=1}^{N}f_k\int_\Omega\frac{\partial\xi_k}{\partial Fo}\xi_i dXdY \tag{32}$$

Table 1
The required time for simulation of approximately 90% of melting versus grid sizes for $Pr = 0.0216$, $Ra = 2.1\times10^5$, Ste = 0.039, $A_{mush} = 1.6\times10^6$.

Cases	Grid size	Run time
Case1	100 × 100	14 h, 21 min
Case2	125 × 125	1 day, 6 h12 min
Case3	150 × 150	2 day, 1 h, 20 min
Case4	175 × 175	2 days, 18 h, 27 min
Case5	200 × 200	3 days, 10 h, 48 min

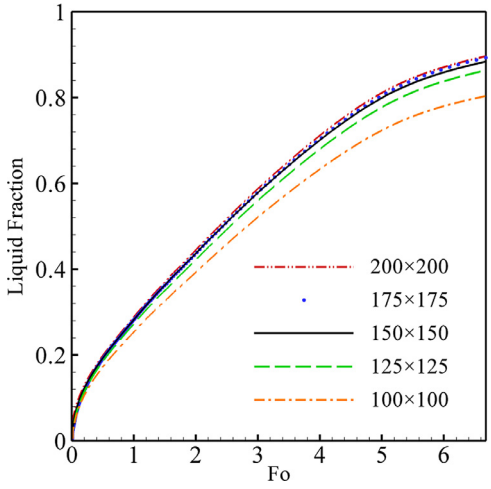

Fig. 2. The liquid fraction for various grid sizes.

4. Validations

4.1. Grid independency test

To check the grid independency of the solution, the case of $Pr = 0.0216$, $Ra = 2.1\times10^5$, Ste = 0.039, $A_{mush} = 1.6\times10^6$ are calculated for several grid sizes as shown in Table 1. This table presents the required time for simulation of approximately 90% of melting for various grid sizes. The calculations are performed using a supercomputer with 40 GB of memory and 20 CPU cores each of 2.2 GHz. In addition, the liquid fraction for different grid sizes is depicted in Fig. 2, which indicates that the grid size of 150 × 150 can provide a tradeoff between the acceptable accuracy and the time consumed by the processor. Hence, the results of the present study are carried out using the grid size 150 × 150.

4.2. Comparisons with others

The reliability of the present solution is further ascertained by solving several previously investigated problems. As a first case, the results of the present study are compared with the experimental results of Gau and Viskanta [52] and the numerical results available in the literature for a rectangular cavity with an aspect ratio (height/width) of 0.714. In the experiment of Gau and Viskanta [52], the left wall is hot while the top and bottom walls are insulated. Gau and Viskanta [52] have evaluated the melting interface using the pour-out method and the probing method. Kashani et al. [28], Khodadadi and Hosseinzadeh [38], Brent et al. [53], Joulin et al. [54], Viswanath and Jaluria [55], Tiari et al. [21] and Desai and Vafai [56] also addressed the evaluated melting interface for this problem numerically. The summary of the available numerical results are plotted in Fig. 3(a) and (b). As seen, the results of the present study are in reasonable agreement with the available experimental and numerical results. In the case of $Fo = 3.48$, the results are somehow different from the experiment but in agreement with the numerical results. The previous authors have concluded that the discrep-

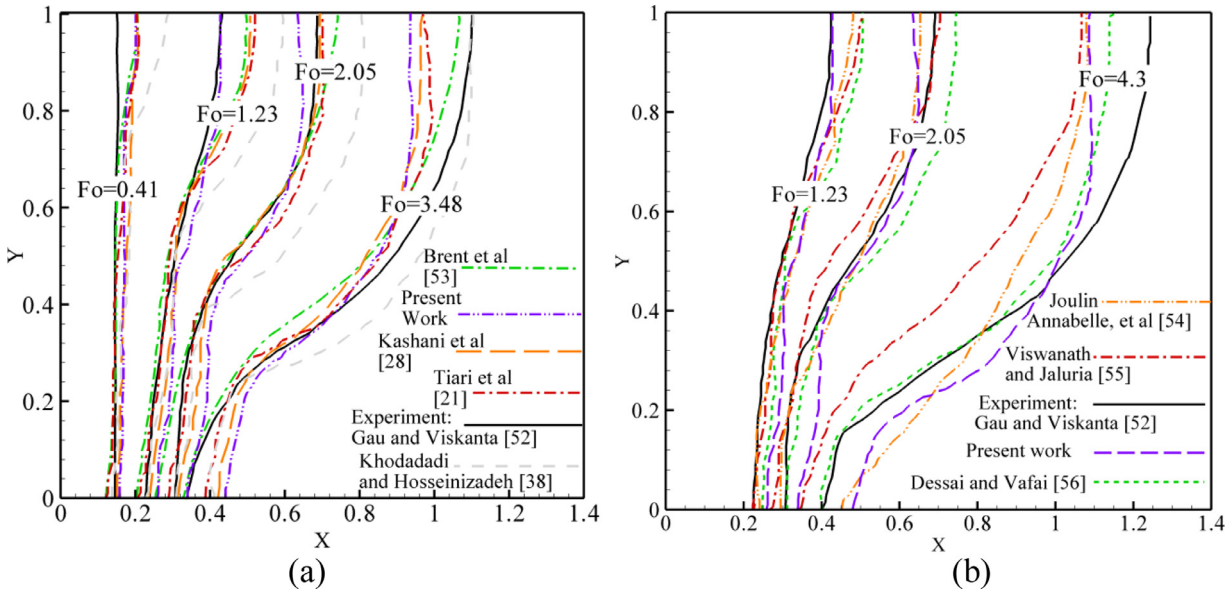

Fig. 3. Comparisons among the experimental measurement of Gau and Viskanta [52] and numerical results available in literature and the results of the present study (a) and (b): uniformly heated at left and cooled at right with adiabatic horizontal walls, $Ra = 6 \times 10^5$ $Pr = 0.0216$.

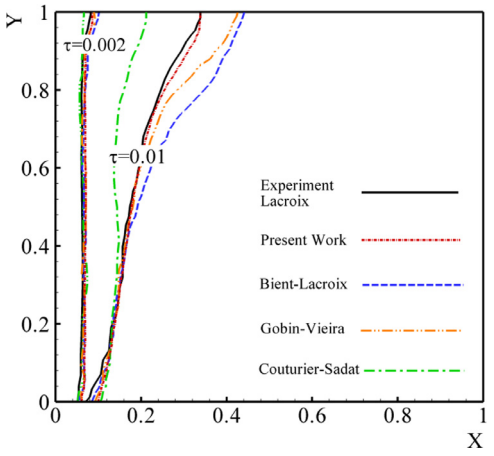

Fig. 4. A comparison between the benchmark study of Bertrand et al. [57] and the results of present study ($\tau = Fo \times Ste$) when $\tau = 2 \times 10^{-3}$ and $\tau = 1 \times 10^{-2}$.

ancy between the numerical and experimental results in this case could be due to the instrumentation and method of evaluating the melting interface in the experiment of Gau and Viskanta [52]. The authors have measured the melting interface mechanically using a manual mechanical probe. For high values of Fo, the solid–liquid interface of melting could be unstable, and hence, distinguishing the precise shape of the interface is hard.

As another validation, the results of the present finite element code are compared with the study of Bertrand et al. [57] when $Ra = 1 \times 10^7$, $Pr = 50$, and $\alpha_s/\alpha_l = 1$. Considering the study of Bertrand et al. [57] as a benchmark, different authors have reported the results of the melting interface for a square cavity. The results are shown in Fig. 4. As seen, there is a good agreement between the results of the present study and the results available in the literature.

As an extra comparison, the results of the present study are compared with the experimental results reported by Kumar et al. [58] for melting of lead. Kumar et al. [58] have examined the melting of lead contained in a stainless steel cuboid. In their study, there was a heater mounted at one of the vertical sidewalls of the cavity, which provided a constant heat flux, while the other walls were insulated. The authors have captured photography of the solid–liquid interface movement during the melting of lead using the neutron radiography. Following the setup and boundary conditions of Kumar et al. [58] and the study of Ghalambaz et al. [59], a comparison between the results of the present study and the experimental results of Kumar et al. [58] for the position of the melting interface is performed at different time steps. The results of this comparison are reported in Table 2. As seen, a good agreement between the results of the present study and those reported by Kumar et al. [58] is obtained.

Sebti et al. [48] have studied the melting of Cu-paraffin phase-change material in a square cavity for various volume fractions of copper nanoparticles. Hence, following the study of Sebti et al. [48], the comparison results of the melting front are reported in Table 3. This table shows the location of the melting interface for two different nanoparticles volume fractions of $\phi = 0\%$ and $\phi = 2.5\%$ at the non-dimensional time step of $Fo = 0.82$. As can be seen, the results of this table show a good agreement between the results of the present study and those reported by Sebti et al. [48].

5. Results and discussion

The present study focuses on the effect of the hybrid nanofluid on the melting characteristics of the paraffin in a two-dimensional square enclosure ($L_x = L_y = 10$ cm). The temperature at the hot wall is fixed at $T_h = 40$ °C, Prandtl number $Pr = 50$, Stefan number Ste = 0.1, Rayleigh number $Ra = 1 \times 10^8$ and the ratio of thermal diffusivities of solid to liquid $\alpha_s/\alpha_l = 1$. Until now, there are no comprehensive mathematical models for the hybrid nanofluid properties. Moreover, models regarding the nanofluids' properties dispersed in PCM give inconsistent behaviors [34]. Therefore, the present computations are based on the linear relations (21)–(24) which have been correlated according to the procedure proposed by Zaraki et al. [49]. This procedure determines its parameters according to experimental data. Table 4 presents the use of data correlation according to several experimental works [50, 60–65]. The range of the volume fraction of nanoparticles has been reported in Table 4. The maximum error of prediction of the results using a linear curve fitting technique was about 6% which is acceptable for most of practical

Table 2
The x coordinate of the melting front as a function of y for different time steps: a comparison between the experimental benchmark results of Kumar et al. [58] and the results of the present study.

$Fo = 1.83$		$Fo = 1.1$		$Fo = 0.73$		y
Present work	Kumar et al. [58]	Present work	Kumar et al. [58]	Present work	Kumar et al. [58]	
0.29	0.29	0.17	0.12	0.13	0.08	0
0.39	0.29	0.19	0.15	0.16	0.09	0.1
0.49	0.40	0.21	0.18	0.16	0.10	0.2
0.55	0.56	0.28	0.23	0.21	0.17	0.3
0.65	0.58	0.30	0.24	0.19	0.17	0.4
0.84	0.78	0.30	0.29	0.21	0.18	0.5
0.95	0.90	0.41	0.37	0.20	0.20	0.6
1	0.98	0.52	0.53	0.27	0.27	0.7
1.06	1.01	0.58	0.57	0.37	0.37	0.8
1.07	1.03	0.57	0.58	0.38	0.40	0.9
1.07	1.03	0.59	0.57	0.38	0.40	1

Table 3
Interface location of solid–liquid (x) at different non-dimensional time ($Fo = 0.82$): a comparison between the result of Sebti et al. [48] and the results of the present study, when (a): $\phi = 0\%$, (b): $\phi = 2.5\%$.

y	(a) $\phi = 0\%$		(b) $\phi = 2.5\%$	
	Present work	Sebti et al. [48]	Present work	Sebti et al. [48]
0	0.30	0.24	0.33	0.26
0.1	0.35	0.32	0.38	0.34
0.2	0.42	0.40	0.45	0.42
0.3	0.50	0.46	0.53	0.50
0.4	0.56	0.54	0.60	0.57
0.5	0.65	0.63	0.70	0.68
0.6	0.76	0.75	0.78	0.80
0.7	0.85	0.85	0.89	0.91
0.8	0.94	0.94	0.96	1
0.9	1	0.99	1	1
1	1	1	1	1

engineering applications. Unfortunately, there are no published experimental data for phase-change hybrid nanofluids, such as paraffin or Octadecane, which are oil-based fluids. Hence, we have not limited our study to correlation parameters of a special case. However, a set of results for high-value correlation parameters has been considered to cover all of the possible ranges of the hybrid nanofluid. In addition, the case studies are also possible using the available experimental data. In the present study, the results of the case study of water/Ag–MgO hybrid NEPCM are reported using the actual experimental data of Esfe et al. [50].

However, the parametric values of the thermal conductivity and the dynamic viscosity parameters are set in many combinations where $Nc = 0$, 5, 18 and $N\nu = 0$, 5, 18. The phase-change material adopted in the present study is Octadecane with its thermo-physical properties listed in Table 5.

Table 4
Results of data correlations for Nc and $N\nu$ using several experimental data.

Case	Refs.	Base fluid	Temperature (°C)	Type	Size (nm)	Shape	Relative fraction	Volume fraction range %	Nc	$N\nu$
1	[50]	Water	–	Ag	25	Disordered	0.5	0–2	21	6.8
				MgO	40	Disordered	0.5			
2	[60]	Water	32	Al_2O_3	17	Spherical	0.9	0.1–2	9.2	33.29
				Cu	17	Spherical	0.1			
3	[61]	Water	20	MWCNT	OD = 10–30 Length = 0.5–500 μm	Cubic	0.74 (g)	0.1–0.3	82.59	122.34
				Fe_3O_4	13	Cubic	0.26 (g)			
4	[61]	Water	40	MWCNT	OD = 10–30 Length = 0.5–500 μm	Cubic	0.74 (g)	0.1–0.3	106.05	132.71
				Fe_3O_4	13	Cubic	0.26 (g)			
5	[62]	EG	30	ZnO	35–45	Spherical	0.5	0–3.5	6.68	–
				TiO_2	30	Spherical	0.5			
6	[62]	EG	40	ZnO	35–45	Spherical	0.5	0–3.5	8.82	–
				TiO_2	30	Spherical	0.5			
7	[63]	Water	60	Cu	55	Spherical	0.5(g)	0.1–2	4.03	–
				TiO_2	55	Spherical	5(g)			
8	[64]	SAE40	25	MWCNTs	ID = 3–5 OD = 5–15	–	0.2	0–2	–	38.62
				SiO_2	20–30	–	0.8			
9	[64]	SAE40	30	MWCNTs	ID = 3–5 OD = 5–15	–	0.2	0–2	–	54.19
				SiO_2	20–30	–	0.8			
10	[65]	EG	30	F-MWCNTs	ID = 3–5 OD = 5–15	–	0.5	0–2.3	10.45	–
				Fe_3O_4	20–30	Spherical	0.5			
11	[65]	EG	40	F-MWCNTs	ID = 3–5 OD = 5–15	–	0.5	0–2.3	13.6	–
				Fe_3O_4	20–30	Spherical	0.5			
12	[65]	EG	50	F-MWCNTs	ID = 3–5 OD = 5–15	–	0.5	0–2.3	18.11	–
				Fe_3O_4	20–30	Spherical	0.5			

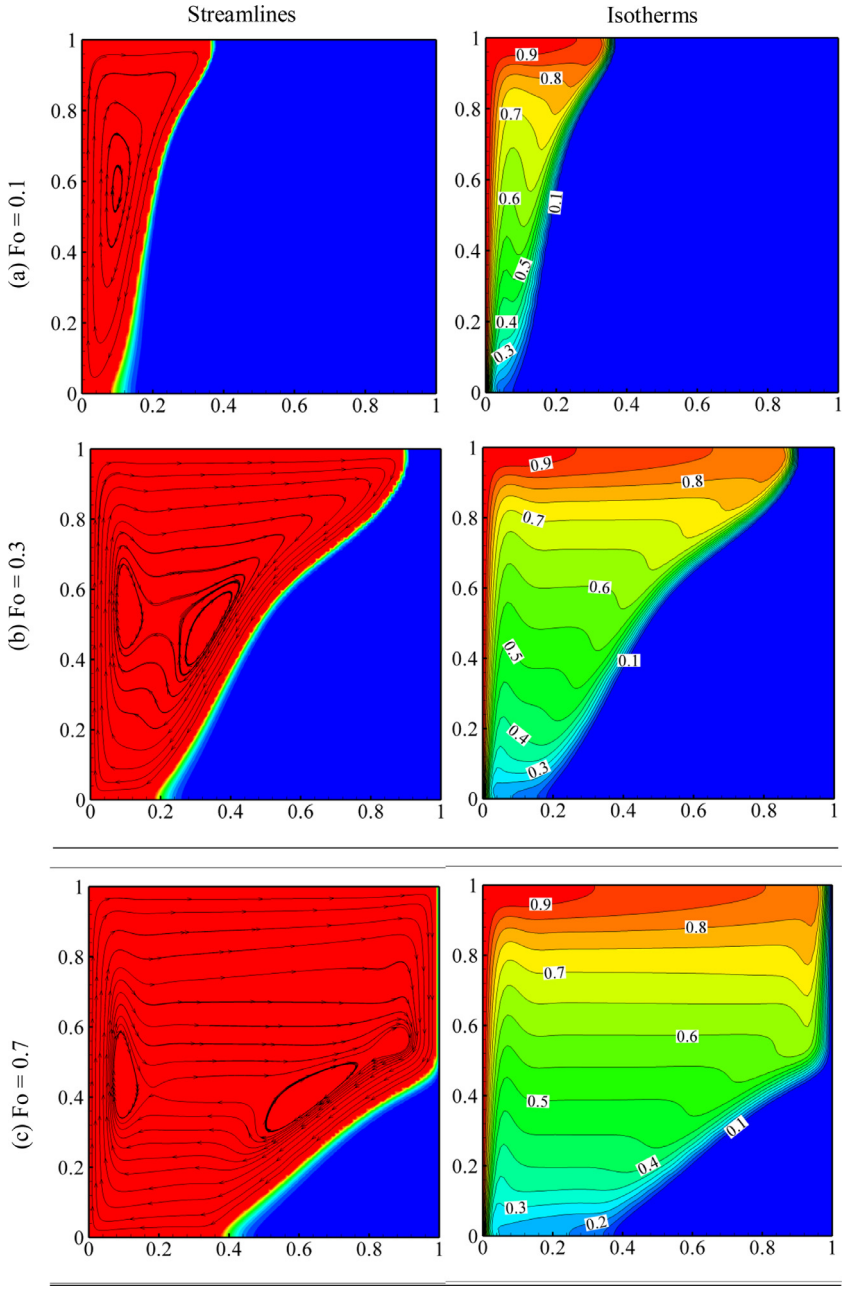

Fig. 5. Streamlines and isotherms for $Nc = 0$, $N\nu = 0$ at (a) $F_o = 0.1$, (b) $F_o = 0.3$, and (c) $F_o = 0.7$.

The evolution of the melting process with dimensionless time Fo is shown in Fig. 5 by the contour maps of the streamlines (on the left) and the isotherms (on the right) for pure Octadecane ($Nc = N\nu = 0$). During the initial stage of melting, where $Fo = 0.1$ (Fig. 5(a)), the molten liquid progresses from the hot left wall with a vertically elongated clockwise rotating vortex. Due to the stronger buoyancy effect close to the top of the cavity, the liquid tends to extend horizontally. Thus, larger molten liquid quantity exists there. In addition, the mushy zone in the top part of the cavity looks thinner than that in the cavity bottom. The corresponding isotherms demonstrate the convection dominance in the upper part of the cavity, where hotter liquid exists there. When *Fo* evolves to 0.3 (Fig. 5(b)), the progressively increasing buoyancy effect produces a double-eye vortex of the melting. Moreover, the hot liquid, which moves up and circulates in the upper part of the cavity, increases the melting rate in the solid, which in turn, rapidly increases the molten liquid quantity and thins the mushy zone when one moves from the bottom part to the top part of the cavity. The molten liquid manifests flatter isotherms in the upper part of the cavity. When further time elapses, (Fig. 5(c)), the liquid in the upper part of the cavity moves strongly in a horizontal

Table 5
Thermo- physical properties of Octadecane.

Property	Symbol	Value	Unit
Density (Solid/Liquid)	ρ	800	(kg/m^3)
Thermal expansion coefficient	β	2×10^{-3}	(1/K)
Fusion temperature	T_f	303.15	(K)
Thermal conductivity (Solid/Liquid)	k	0.2	(W/m K)
Latent heat of fusion	L	$1.25 \times 10^{+5}$	(J/kg)
Specific heat capacity (Solid/Liquid)	C	1250	(J/kg K)
Dynamic viscosity	μ	8×10^{-3}	(kg/m s)

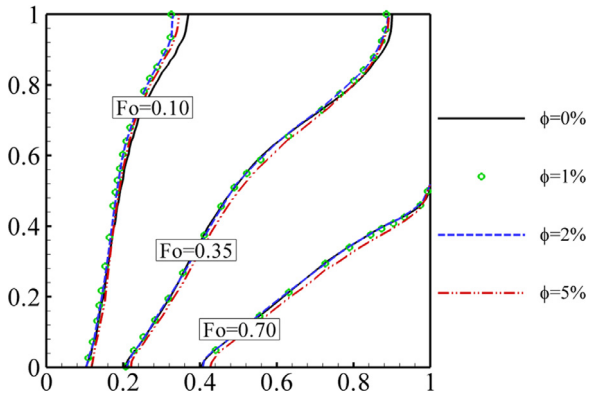

Fig. 6. The melting interface for $Nc = 5$, $Nv = 18$.

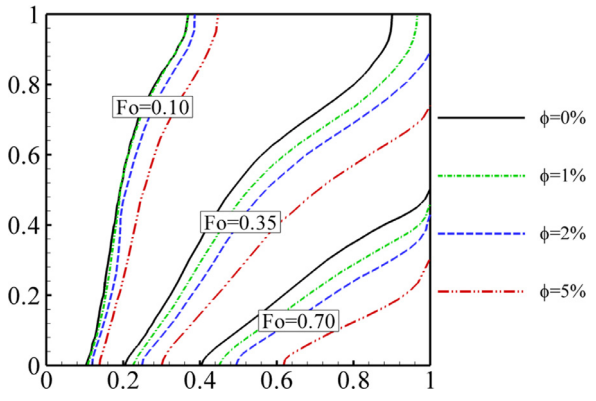

Fig. 7. The melting interface for $Nc = 18$, $Nv = 18$.

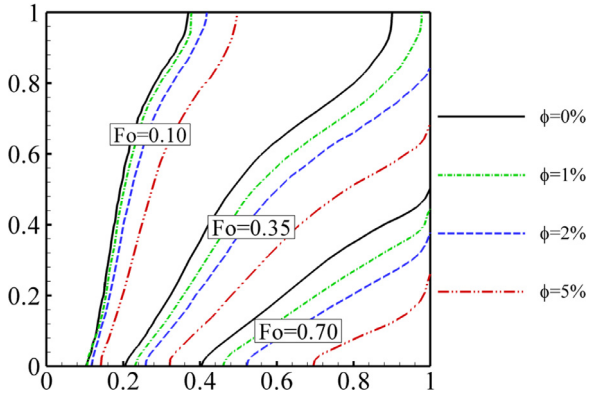

Fig. 8. The melting interface for $Nc = 18$, $Nv = 5$.

manner. As a result, most solid melts leaving a triangular solid quantity in the lower left corner, i.e. the solid–liquid interface is mostly linear with mostly homogeneous mushy zone thickness. The isotherms imply a purely convective heat transfer within the middle of the cavity, while close to the left hot wall, high temperature gradients exist which indicates a horizontal heat transfer. However, at all times (Fig. 5(a)–(c)), the temperature within the solid phase is homogenous.

Figs. 6–8 present the melting interface that is traced within three values of the dimensionless time Fo (0.1, 0.35, 0.7) for different total nanoparticles volume fraction ϕ (0, 1%, 2%, 5%), where each figure is plotted for a selected combination of the correlation parameters. In the combination parameters of $Nc = 5$ and $Nv = 18$ (Fig. 6), the dynamic viscosity of the hybrid nanofluid is robustly enhanced greater than the enhancement of the thermal conductivity. As such, at the earlier times ($Fo = 0.1$ and 0.35), the role of the thermal conductivity can be seen

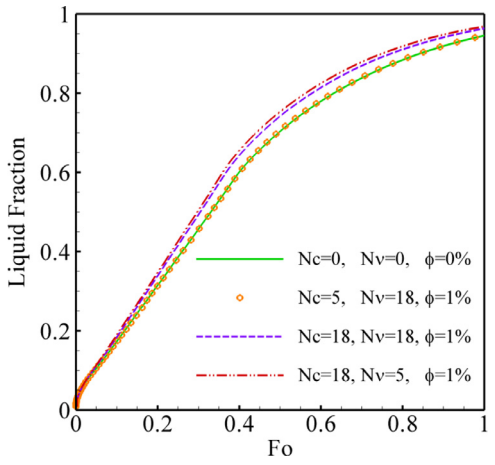

Fig. 9. Effect of $\phi = 1\%$ volume fraction of nano-hybrid on liquid fraction for various Nc and Nv.

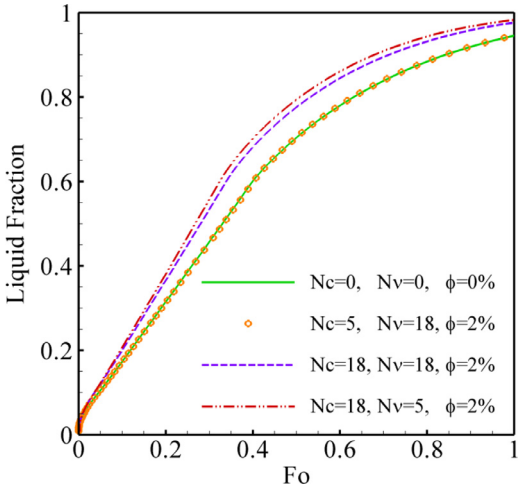

Fig. 10. Effect of $\phi = 2\%$ volume fraction of nano-hybrid on liquid fraction for various Nc and Nv.

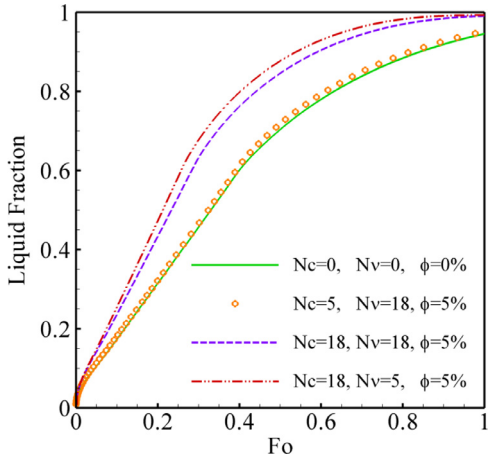

Fig. 11. Effect of $\phi = 5\%$ volume fraction of nano-hybrid on liquid fraction for various Nc and Nv.

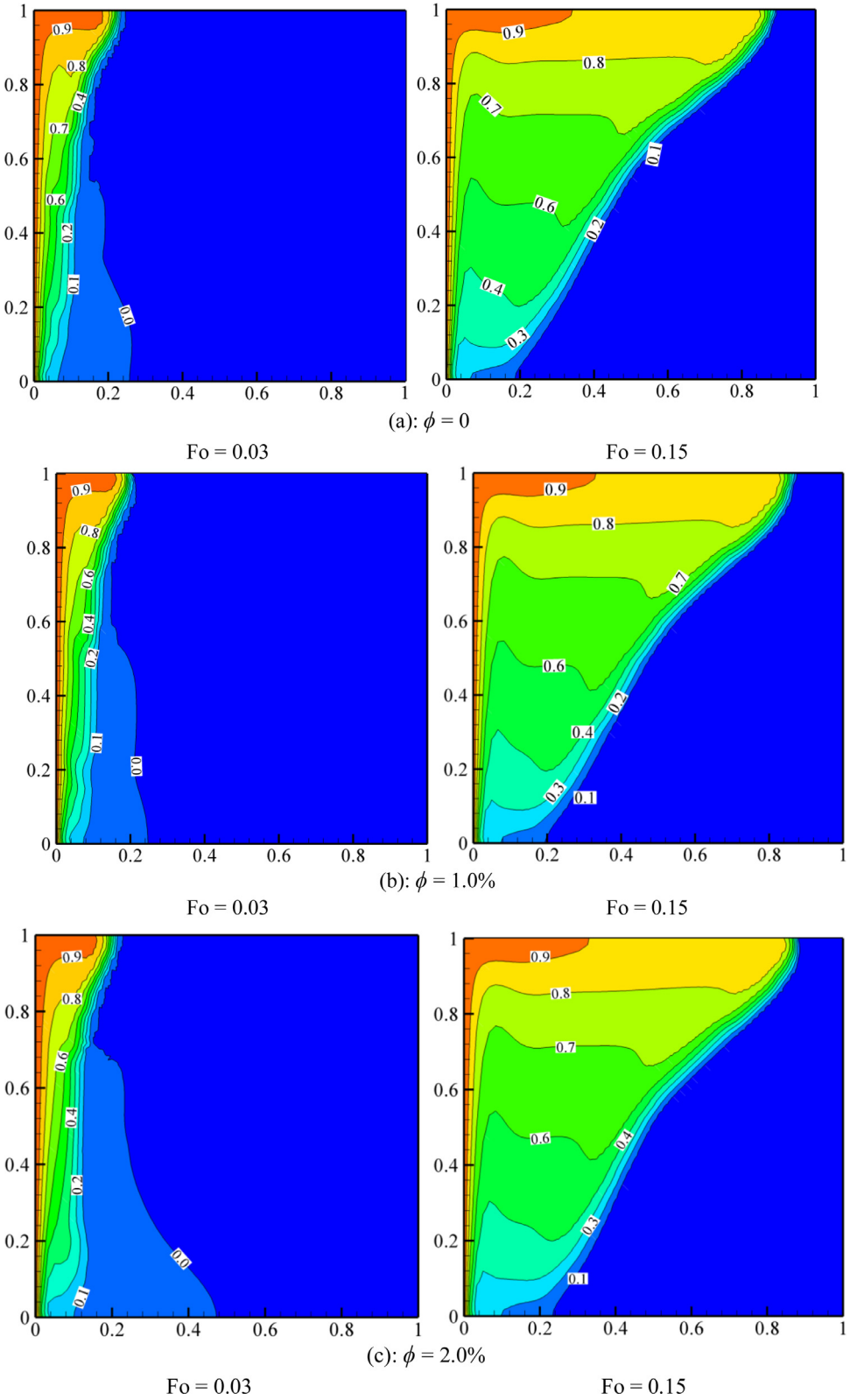

Fig. 12. Isotherms for ϕ = 0, 0.1, 0.2 at F_o = 0.03 and 0.15: the case study of for water/Ag–MgO NEPCM.

in the lower part of the melting interface, where a slight progress takes place by increasing ϕ. This refers to the conduction dominance in this region. However, in the upper part of the cavity, the role of the viscous force restricts the available strong circulation and hence, resulting in a lag in the melting interface with increasing values of ϕ. This mechanism can result in a planer-melting interface. When *Fo* = 0.7, the flow adjacent to the mostly linear melting interface is due to gravity (as shown in Fig. 5(c)) and the thickness of the mushy zone is approximately homogenous, thus, the viscous force effect will be weak against the ther-

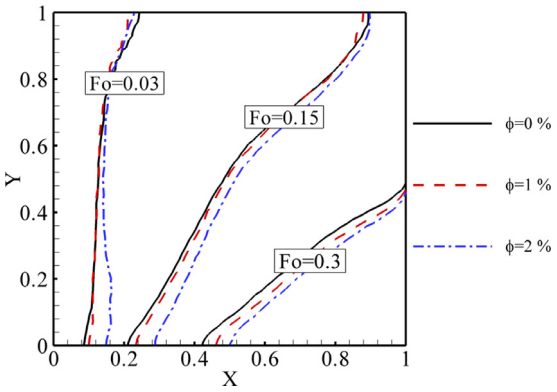

Fig. 13. The melting interface curves of water/Ag–MgO hybrid NEPCM for various values of volume fraction of hybrid nanoparticles.

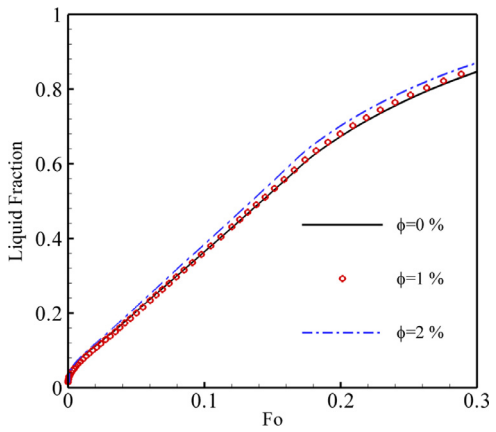

Fig. 14. Effect of ϕ on the volume fraction of molten water/Ag–MgO hybrid NEPCM.

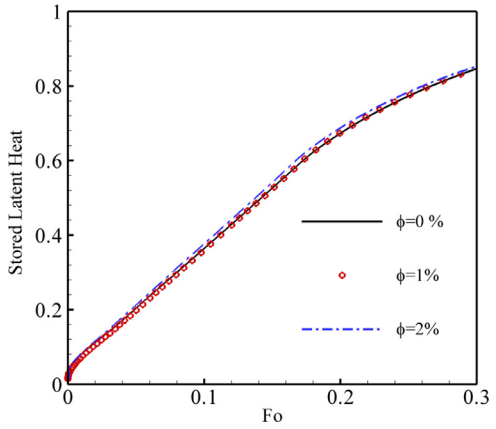

Fig. 15. Effect of ϕ on stored latent heat of water/Ag–MgO hybrid NEPCM.

mal energy gained due to nanoparticles loading by 5%. Therefore, a homogenous progress of the melting interface can be seen in Fig. 6.

There are cases in which *Nc* is greater than *Nv* for instance *Nc* in Case 1 reported in Table 4 is higher than *Nv*, i.e. $Nc = 21$ and $Nv = 6.8$. In addition, for some cases such as Cases 8 and 9 in Table 4, the value of *Nc* is not available. Hence, in the present analysis, we have also studied the cases in which *Nc* values are higher than *Nv*. We believe that presenting such results for high values of *Nc* are essential for future studies to show researchers how much enhancement in *Nc* (compared to *Nv*) is required for overall enhancement in the overall melting volume fraction and the overall heat release and the melting behavior of NEPCMs. Indeed, such cases are of more interest for heat transfer applications of NEPCMs.

Fig. 7 shows that when the parameters *Nc* and *Nv* are set to 18 and 18, a significant progress of the melting interface takes place with nanoparticles loading even at the initial melting process. However, the melting rate is higher with time evolution. This is because the significantly-enhanced thermal conductivity can decrease the latent heats of fusion and consequently, increases the melting rate. The melting configurations of $Nc = 18$ and $Nv = 5$ are presented in Fig. 8. Altogether, there are no significant changes with the previous combination set ($Nc = Nv = 18$) except that at $Fo = 0.7$, the melting rate is faster. According to these two figures, it can be demonstrated that in a phase-change material, the effect of the thermal conductivity manifests the dominance role in accelerating the melting process. Moreover, it is worth mentioning that the melting configuration with increasing the loading ratio of the hybrid nanoparticles agrees with the finding of the experimental study of Zeng et al. [27].

The traced liquid fraction in the PCM is depicted in Figs. 9–11 for different parameters combinations and different loading volume fractions of the hybrid nanofluid. Initially, the nanoparticles have no influencing role on the liquid fraction in the cavity. As time goes on, prominent increase of the liquid fraction is associated with increasing the volume fraction of the hybrid nanoparticles. Moreover, the increase in the liquid fraction is distinguished when the thermo-physical properties of the hybrid nanofluid are governed by a higher parameter of the thermal conductivity as shown in Fig. 11, where higher liquid fractions available with setting the thermal conductivity parameter to $Nc = 18$.

Now, the importance of Table 4 becomes evident. That is, the hybrid nanofluids which have *Nc* much greater than *Nv* or say equivalent values, are expected to melt faster than those having $Nv \gg Nc$. Thus, the hybrid nanoparticles configuration of Esfe et al. [49], which uses Mg–MgO, dispersed in water can be considered as having a great chance in accelerating the melting process.

As a case study, the exact values of the non-dimensional parameters such as ρ_{bf}/ρ_{hnf}, $(\rho C_p)_{bf}/(\rho C_p)_{hnf}$, C_{bf}/C_{hnf} and $\rho_{bf}\beta_{bf}/(\rho\beta)_{hnf}$ were adopted from the experimental study of Esfe et al. [50]. The values of *Nc* and *Nv* have been reported in Table 4 as $Nc = 21$ and $Nv = 6.8$.

Fig. 12 illustrates the isotherms for the case study of water/Ag–MgO NEPCM at two time steps of $Fo = 0.03$ and $Fo = 15$ for various volume fractions of $\phi = 0\%$, 1.0% and 2.0%. For the initial stages of the melting process, i.e. $Fo = 0.03$, a comparison between the isotherms due to different volume fractions of nanoparticles reveals that the most differences can be observed in the regions near the bottom of the cavity. This is where the convective heat transfer mechanism is weak and the diffusive heat transfer mechanism is the dominant mode. For higher Fourier numbers, i.e. $Fo = 0.15$, the effect of the presence of nanoparticles on the temperature profiles is slightly developed in the bottom areas into the middle regions of the cavity. In order to show the effect of the presence of nanoparticles on the melting front interface, the melting volume fraction and the stored latent heat (Q/L) for the case study of water/Ag–MgO NEPCM are plotted in Figs. 13–15. As can be seen, the greatest difference in the melting front interfaces is at the bottom of the cavity. At the bottom of the cavity, the fluid is trapped between the hot wall and the melt interface where the velocities are small. Hence, the heat transfer takes place mainly by conduction. As the presence of the nanoparticles would significantly enhance the thermal conductivity of the NEPCM, i.e. $Nc = 21$, the most significant difference between the melting front interfaces can also be seen at the bottom of the cavity. In the top regions, where the fluid can move more freely, the convective mechanism gets important. As discussed, the presence of nanoparticles mainly affects the thermal conductivity and the dynamic viscosity of the NEPCM. Thus, the increase of the thermal conductivity tends to accelerate the melting process but the increase of the dynamic viscosity tends to suppress the convection mechanism. As a result, the change in the melting front curves due to the increment of the nanoparticles volume fractions is not much significant in the top region of the cavity. Fig. 14 shows

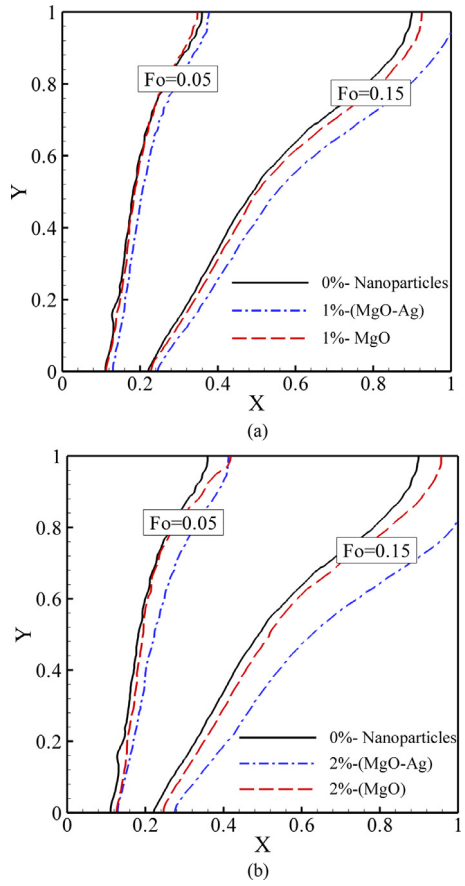

Fig. 16. A comparison between the melting interface curves of the water as the base fluid, water/Ag–MgO hybrid NEPCM, and single water/MgO NEPCM for: (a) 1% total volume fraction of nanoparticles and (b) 2% total volume fraction of nanoparticles.

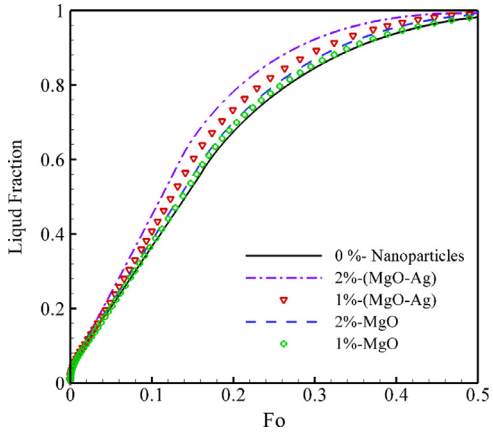

Fig. 17. A comparison between the liquid fractions of the water as the base fluid, water/Ag–MgO hybrid NEPCM, and single water/MgO NEPCM.

that the increase of the volume fraction of Ag–MgO nanoparticles would enhance the melting fraction. However, as the presence of nanoparticles would reduce the stored latent heat, Fig. 15 demonstrates little enhancement in the release of stored latent heat of NEPCMs due to the presence of Ag–MgO nanoparticles.

Fig. 16 compares the effect of using a single NEPCM (water/MgO) and a hybrid NEPCM (water/Ag–MgO) on the melting interface curves for 1% and 2% total volume fractions of nanoparticles. The utilized thermophysical properties are given in Table 4. The results are reported for two non-dimensional times of $Fo = 0.05$ and $Fo = 0.15$. The results confirm that the melting process has enhanced by using a hybrid NEPCM in all studied cases. Indeed, in all cases, the melting interface of the hybrid NEPCM has further advanced toward the cold wall. Fig. 17 depicts the liquid fraction of NEPCMs for the studied cases of Fig. 16 as a function of the non-dimensional time (*Fo*). This figure is in agreement with Fig. 16 and shows that by using the hybrid NEPCM, the fusion time has been improved.

6. Conclusions

Melting of nanoparticles-enhanced phase-change materials has been numerically analyzed using the finite element method. The enhancement utilizes the hybrid nanofluid strategy. A linearized correlations procedure is followed to determine the properties of the hybrid nanofluid. The impacts of the nanoparticles' volume fraction and various models' parameters on the melting behavior have been traced with time. The results have led us to report the following conclusions:

- The used linearized models give a melting behavior which completely agrees with the finding of the available experimental data associated with nanoparticles-enhanced phase-change materials.
- The melting process expedites tremendously when the enhancement in the thermal conductivity is much greater than the enhancement of the dynamic viscosity.
- Marginal variations in the liquid fraction are predicted when the enhancement of the dynamic viscosity is much greater than the thermal conductivity enhancement.
- According to the available experimental data, hybrid nanoparticles composed of Ag–MgO demonstrates the best fusion performance.
- At the initial melting stages, the mushy zone is thicker in the lower part of the solid–liquid interface where the convection is too small. With time evolution, the mushy zone tends to be homogenous in thickness.
- The case study of water containing Ag (25 nm)–MgO (40 nm) nanoparticles demonstrates small enhancements in the acceleration of the melting fraction and the release of latent heat.
- Using a water/Ag–MgO hybrid NEPCM shows a faster fusion time compared to the single water/MgO NEPCM.

It should be mentioned that one of the most important aspect of NEPCMs is the size of nanoparticles and their composition as it could significantly affect the convective behavior of NEPCM in the melting process and the release rate of latent heat.

Acknowledgments

The first and second authors acknowledge the financial support of Dezful Branch, Islamic Azad University, Dezful, Iran. Ghalambaz and Doostani are also greatful to National Iranian Drilling Company (NIDC) and Marun Petrochemical Company (MPC) for the curcial support of the present study. The authors are thankful to Sheikh Bahaei National High Performance Computing Center (SBNHPCC) for providing computational resources, supported by the scientific and technological department of the presidential office and Isfahan University of Technology (IUT).

References

[1] Regin AF, Solanki S, Saini J. Heat transfer characteristics of thermal energy storage system using PCM capsules: a review. Renew Sustain Energy Rev 2008;12(9):2438–58.
[2] Telkes M, Raymond E. Storing solar heat in chemicals- a report on the dover house. Heat Vent 1949;46(11):80–6.
[3] Telkes M. Thermal energy storage in salt hydrates. Sol Energy Mater 1980;2(4):381–93.
[4] Telkes M. Thermal storage for solar heating and cooling. In: Proceedings of the workshop on solar energy storage subsystems for the heating and cooling of buildings. Charlottesville, Virginia, USA; 1975.
[5] Telkes M. Trombe wall with phase change storage material. In: Proceedings of the 2nd national passive solar conference. Philadelphia, PA, USA; 1978.

[6] Zhou D, Zhao C-Y, Tian Y. Review on thermal energy storage with phase change materials (PCMs) in building applications. Appl Energy 2012;92:593–605.
[7] Agyenim F, Hewitt N, Eames P, Smyth M. A review of materials, heat transfer and phase change problem formulation for latent heat thermal energy storage systems (LHTESS). Renew Sustain Energy Rev 2010;14(2):615–28.
[8] Sharma A, Tyagi VV, Chen C, Buddhi D. Review on thermal energy storage with phase change materials and applications. Renew Sustain Energy Rev 2009;13(2):318–45.
[9] Khan Z, Khan Z, Ghafoor A. A review of performance enhancement of PCM based latent heat storage system within the context of materials, thermal stability and compatibility. Energy Convers Manag 2016;115:132–58.
[10] Fan L, Khodadadi JM. Thermal conductivity enhancement of phase change materials for thermal energy storage: a review. Renew Sustain Energy Rev 2011;15(1):24–46.
[11] Liu L, Su D, Tang Y, Fang G. Thermal conductivity enhancement of phase change materials for thermal energy storage: a review. Renew Sustain Energy Rev 2016;62:305–17.
[12] Samarskii A, Vabishchevich P, Iliev O, Churbanov A. Numerical simulation of convection/diffusion phase change problems – a review. Int J Heat Mass Transf 1993;36(17):4095–106.
[13] Hu H, Argyropoulos SA. Mathematical modelling of solidification and melting: a review. Model Simul Mater Sci Eng 1996;4(4):371.
[14] Ebrahimnia-Bajestan E, Niazmand H, Etminan-Farooji V, Ebrahimnia E. Numerical modeling of the freezing of a porous humid food inside a cavity due to natural convection. Numer Heat Transf Part A Appl 2012;62(3):250–69.
[15] Allen MJ, Sharifi N, Faghri A, Bergman TL. Effect of inclination angle during melting and solidification of a phase change material using a combined heat pipe-metal foam or foil configuration. Int J Heat Mass Transf 2015;80:767–80.
[16] Mirzaei H, Dadvand A, Mastiani M, Sebti SS, Kashani S. Melting of a phase change material in a horizontal annulus with discrete heat sources. Therm Sci 2015;19(5):1733–45.
[17] Kousksou T, Mahdaoui M, Ahmed A, Msaad AA. Melting over a wavy surface in a rectangular cavity heated from below. Energy 2014;64:212–19.
[18] Bondareva N, Sheremet M. Mathematical simulation of melting inside a square cavity with a local heat source. Thermophys Aeromech 2016;23(4):553–65.
[19] Bondareva NS, Sheremet MA. Effect of inclined magnetic field on natural convection melting in a square cavity with a local heat source. J Magn Magn Mater 2016;419:476–84.
[20] Bondareva NS, Sheremet MA. Natural convection heat transfer combined with melting process in a cubical cavity under the effects of uniform inclined magnetic field and local heat source. Int J Heat Mass Transf 2017;108:1057–67.
[21] Tiari S, Qiu S, Mahdavi M. Numerical study of finned heat pipe-assisted thermal energy storage system with high temperature phase change material. Energy Conver Manag 2015;89:833–42.
[22] Tiari S, Qiu S, Mahdavi M. Discharging process of a finned heat pipe-assisted thermal energy storage system with high temperature phase change material. Energy Conver Manag 2016;118:426–37.
[23] Tiari S, Mahdavi M, Qiu S. Experimental investigation of a heat pipe-assisted latent heat thermal energy storage system. In: Proceedings of the APS division of fluid dynamics meeting abstracts; 2016.
[24] Sarı A, Karaipekli A. Thermal conductivity and latent heat thermal energy storage characteristics of paraffin/expanded graphite composite as phase change material. Appl Therm Eng 2007;27(8):1271–7.
[25] Motahar S, Alemrajabi AA, Khodabandeh R. Experimental study on solidification process of a phase change material containing TiO_2 nanoparticles for thermal energy storage. Energy Conver Manag 2017;138:162–70.
[26] Dhaidan NS. Nanostructures assisted melting of phase change materials in various cavities. Appl Therm Eng 2017;111:193–212.
[27] Şahan N, Fois M, Paksoy H. Improving thermal conductivity phase change materials – a study of paraffin nanomagnetite composites. Sol Energy Mater Sol Cells 2015;137:61–7.
[28] Kashani S, Ranjbar A, Abdollahzadeh M, Sebti S. Solidification of nano-enhanced phase change material (NEPCM) in a wavy cavity. Heat Mass Transf 2012;48(7):1155–66.
[29] Abdollahzadeh M, Esmaeilpour M. Enhancement of phase change material (PCM) based latent heat storage system with nano fluid and wavy surface. Int J Heat Mass Transf 2015;80:376–85.
[30] Jourabian M, Farhadi M. Melting of nanoparticles-enhanced phase change material (NEPCM) in vertical semicircle enclosure: numerical study. J Mech Sci Technol 2015;29(9):3819–30.
[31] Sharma R, Ganesan P, Sahu J, Metselaar H, Mahlia T. Numerical study for enhancement of solidification of phase change materials using trapezoidal cavity. Powder Technol 2014;268:38–47.
[32] Trp A. An experimental and numerical investigation of heat transfer during technical grade paraffin melting and solidification in a shell-and-tube latent thermal energy storage unit. Sol Energy 2005;79(6):648–60.
[33] Ho C, Gao J. An experimental study on melting heat transfer of paraffin dispersed with Al_2O_3 nanoparticles in a vertical enclosure. Int J Heat Mass Transf 2013;62:2–8.
[34] Zeng Y, Fan L-W, Xiao Y-Q, Yu Z-T, Cen K-F. An experimental investigation of melting of nanoparticle-enhanced phase change materials (NePCMs) in a bottom-heated vertical cylindrical cavity. Int J Heat Mass Transf 2013;66:111–17.
[35] Motahar S, Nikkam N, Alemrajabi AA, Khodabandeh R, Toprak MS, Muhammed M. A novel phase change material containing mesoporous silica nanoparticles for thermal storage: a study on thermal conductivity and viscosity. Int Commun Heat Mass Transf 2014;56:114–20.
[36] Nourani M, Hamdami N, Keramat J, Moheb A, Shahedi M. Thermal behavior of paraffin-nano-Al_2O_3 stabilized by sodium stearoyl lactylate as a stable phase change material with high thermal conductivity. Renew Energy 2016;88:474–82.
[37] Fan L-W, Zhu Z-Q, Zeng Y, Ding Q, Liu M-J. Unconstrained melting heat transfer in a spherical container revisited in the presence of nano-enhanced phase change materials (NePCM). Int J Heat Mass Transf 2016;95:1057–69.
[38] Khodadadi J, Hosseinizadeh S. Nanoparticle-enhanced phase change materials (NEPCM) with great potential for improved thermal energy storage. Int Commun Heat Mass Transf 2007;34(5):534–43.
[39] Wu S, Wang H, Xiao S, Zhu D. Numerical simulation on thermal energy storage behavior of Cu/paraffin nanofluids PCMs. Procedia Eng 2012;31:240–4.
[40] Ebrahimi A, Dadvand A. Simulation of melting of a nano-enhanced phase change material (NePCM) in a square cavity with two heat source–sink pairs. Alex Eng J 2015;54(4):1003–17.
[41] Han Z, Yang B, Kim S, Zachariah M. Application of hybrid sphere/carbon nanotube particles in nanofluids. Nanotechnology 2007;18(10):105701.
[42] Jana S, Salehi-Khojin A, Zhong W-H. Enhancement of fluid thermal conductivity by the addition of single and hybrid nano-additives. Thermochim Acta 2007;462(1):45–55.
[43] Paul G, Philip J, Raj B, Das PK, Manna I. Synthesis, characterization, and thermal property measurement of nano-$Al_{95}Zn_{05}$ dispersed nanofluid prepared by a two-step process. Int J Heat Mass Transf 2011;54(15):3783–8.
[44] Sarkar J, Ghosh P, Adil A. A review on hybrid nanofluids: recent research, development and applications. Renew Sustain Energy Rev 2015;43:164–77.
[45] Ho C, Huang J, Tsai P, Yang Y. Preparation and properties of hybrid water-based suspension of Al_2O_3 nanoparticles and MEPCM particles as functional forced convection fluid. Int Commun Heat Mass Transf 2010;37(5):490–4.
[46] Botha SS, Ndungu P, Bladergroen BJ. Physicochemical properties of oil-based nanofluids containing hybrid structures of silver nanoparticles supported on silica. Ind Eng Chem Res 2011;50(6):3071–7.
[47] Levin M, Miller M. Maxwell a treatise on electricity and magnetism. Uspekhi Fizicheskikh Nauk 1981;135(3):425–40.
[48] Sebti SS, Mastiani M, Mirzaei H, Dadvand A, Kashani S, Hosseini SA. Numerical study of the melting of nano-enhanced phase change material in a square cavity. J Zhejiang Univ Sci A 2013;14(5):307–16.
[49] Zaraki A, Ghalambaz M, Chamkha AJ, Ghalambaz M, De Rossi D. Theoretical analysis of natural convection boundary layer heat and mass transfer of nanofluids: effects of size, shape and type of nanoparticles, type of base fluid and working temperature. Adv Powder Technol 2015;26(3):935–46.
[50] Esfe MH, Arani AAA, Rezaie M, Yan W-M, Karimipour A. Experimental determination of thermal conductivity and dynamic viscosity of Ag–MgO/water hybrid nanofluid. Int Commun Heat Mass Transf 2015;66:189–95.
[51] Reddy JN. An introduction to the finite element method. New York: McGraw-Hill; 1993.
[52] Gau C, Viskanta R. Melting and solidification of a pure metal on a vertical wall. J Heat Transf 1986;108(1):174–81.
[53] Brent A, Voller V, Reid K. Enthalpy-porosity technique for modeling convection-diffusion phase change: application to the melting of a pure metal. Numer Heat Transf Part A Appl 1988;13(3):297–318.
[54] Joulin A, Younsi Z, Zalewski L, Rousse DR, Lassue S. A numerical study of the melting of phase change material heated from a vertical wall of a rectangular enclosure. Int J Comput Fluid Dyn 2009;23(7):553–66.
[55] Viswanath R, Jaluria Y. A comparison of different solution methodologies for melting and solidification problems in enclosures. Numer Heat Transf Part B Fundam 1993;24(1):77–105.
[56] Desai C, Vafai K. A unified examination of the melting process within a two-dimensional rectangular cavity. J Heat Transf 1993;115(4):1072–5.
[57] Bertrand O, Binet B, Combeau H, Couturier S, Delannoy Y, Gobin D. Melting driven by natural convection a comparison exercise: first results. Int J Therm Sci 1999;38(1):5–26.
[58] Kumar L, Manjunath B, Patel R, Markandeya S, Agrawal R, Agrawal A. Experimental investigations on melting of lead in a cuboid with constant heat flux boundary condition using thermal neutron radiography. Int J Therm Sci 2012;61:15–27.
[59] Ghalambaz M, Doostanidezfuli A, Zargartalebi H, Chamkha AJ. MHD phase change heat transfer in an inclined enclosure: effect of a magnetic field and cavity inclination. Numer Heat Transf Part A Appl 2017;71(1):91–109.
[60] Suresh S, Venkitaraj K, Selvakumar P, Chandrasekar M. Synthesis of Al_2O_3–Cu/water hybrid nanofluids using two step method and its thermo physical properties. Colloids Surf Physicochem Eng Asp 2011;388(1):41–8.
[61] Sundar LS, Singh MK, Sousa AC. Enhanced heat transfer and friction factor of MWCNT–Fe_3O_4/water hybrid nanofluids. Int Commun Heat Mass Transf 2014;52:73–83.
[62] Toghraie D, Chaharsoghi VA, Afrand M. Measurement of thermal conductivity of ZnO–TiO_2/EG hybrid nanofluid. J Therm Anal Calorim 2016;125(1):527–35.
[63] Madhesh D, Parameshwaran R, Kalaiselvam S. Experimental investigation on convective heat transfer and rheological characteristics of Cu–TiO_2 hybrid nanofluids. Exp Therm Fluid Sci 2014;52:104–15.
[64] Esfe MH, Afrand M, Yan W-M, Yarmand H, Toghraie D, Dahari M. Effects of temperature and concentration on rheological behavior of MWCNTs/SiO_2 (20–80)-SAE40 hybrid nano-lubricant. Int Commun Heat Mass Transf 2016;76:133–8.
[65] Harandi SS, Karimipour A, Afrand M, Akbari M, D'Orazio A. An experimental study on thermal conductivity of F-MWCNTs–Fe_3O_4/EG hybrid nanofluid: effects of temperature and concentration. Int Commun Heat Mass Transf 2016;76:171–7.